Detailed structural and biochemical characterization of the nexin-dynein regulatory complex

Toshiyuki Oda, Haruaki Yanagisawa, and Masahide Kikkawa
Department of Cell Biology and Anatomy, Graduate School of Medicine, University of Tokyo, 7-3-1 Hongo Bunkyo-ku, Tokyo 113-0033, Japan

ABSTRACT **The nexin-dynein regulatory complex (N-DRC) forms a cross-bridge between the outer doublet microtubules of the axoneme and regulates dynein motor activity in cilia/flagella. Although the molecular composition and the three-dimensional structure of N-DRC have been studied using mutant strains lacking N-DRC subunits, more accurate approaches are necessary to characterize the structure and function of N-DRC. In this study, we precisely localized DRC1, DRC2, and DRC4 using cryo–electron tomography and structural labeling. All three N-DRC subunits had elongated conformations and spanned the length of N-DRC. Furthermore, we purified N-DRC and characterized its microtubule-binding properties. Purified N-DRC bound to the microtubule and partially inhibited microtubule sliding driven by the outer dynein arms (ODAs). Of interest, microtubule sliding was observed even in the presence of fourfold molar excess of N-DRC relative to ODA. These results provide insights into the role of N-DRC in generating the beating motions of cilia/flagella.**

Monitoring Editor
Wallace Marshall
University of California,
San Francisco

Received: Sep 30, 2014
Revised: Nov 13, 2014
Accepted: Nov 13, 2014

INTRODUCTION

Cilia and flagella are elaborate motile organelles that generate fluid flow with beating motion and play crucial roles in mammalian development (Haimo and Rosenbaum, 1981; Pazour and Rosenbaum, 2002; Kikkawa, 2013). Defects in ciliary/flagellar motility result in primary ciliary dyskinesia (PCD), which is characterized by situs inversus, chronic airway infections, and male infertility (Badano *et al.*, 2006; Fliegauf *et al.*, 2007; Drummond, 2012). Most cilia and flagella have the "9+2" configuration of microtubules, in which the nine outer doublet microtubules (DMTs) appear to be cross-linked by the nexin-dynein regulatory complex (N-DRC; Heuser *et al.*, 2009). N-DRCs are connected to the outer dynein arms (ODAs) via the outer–inner dynein linkers and regulate both ODAs and inner dynein arms (IDAs; Oda *et al.*, 2013). Mutations in N-DRC subunits cause flagellar motility defects (Huang *et al.*, 1982; Gardner *et al.*, 1994) and result in PCD (Austin-Tse *et al.*, 2013; Wirschell *et al.*, 2013). The protein composition and structural configuration of N-DRC have been investigated structurally and biochemically (Heuser *et al.*, 2009; Lin *et al.*, 2011; Bower *et al.*, 2013). The proposed organization of DRC subunits is derived from a comparison between the axonemal structures of wild-type and mutant *Chlamydomonas* strains with partial deficiency in N-DRC components. Although component-deficient mutant strains are powerful models to study the nature of the protein complex, caution is required when interpreting the data because structural deficiency can cause unexpected rearrangement of the target complex. To overcome this problem, we developed a new structural labeling method for cryo–electron tomography (cryo-ET) using the biotin-streptavidin system and identified the three-dimensional (3D) positions of ODA and radial spoke subunits (Oda and Kikkawa, 2013; Oda *et al.*, 2014b). In this study, we applied this structural labeling method to N-DRC. We also purified N-DRC using gel-filtration and ion-exchange chromatography and characterized the composition, structure, and microtubule-binding properties of purified N-DRC.

The authors declare no competing financial interests.

Address correspondence to: Toshiyuki Oda (tooda@m.u-tokyo.ac.jp).

Abbreviations used: BCCP, biotin carboxyl carrier protein; cryo-ET, cryo–electron tomography; DMT, outer doublet microtubule; N-DRC, nexin-dynein regulatory complex; ODA, outer dynein arm.

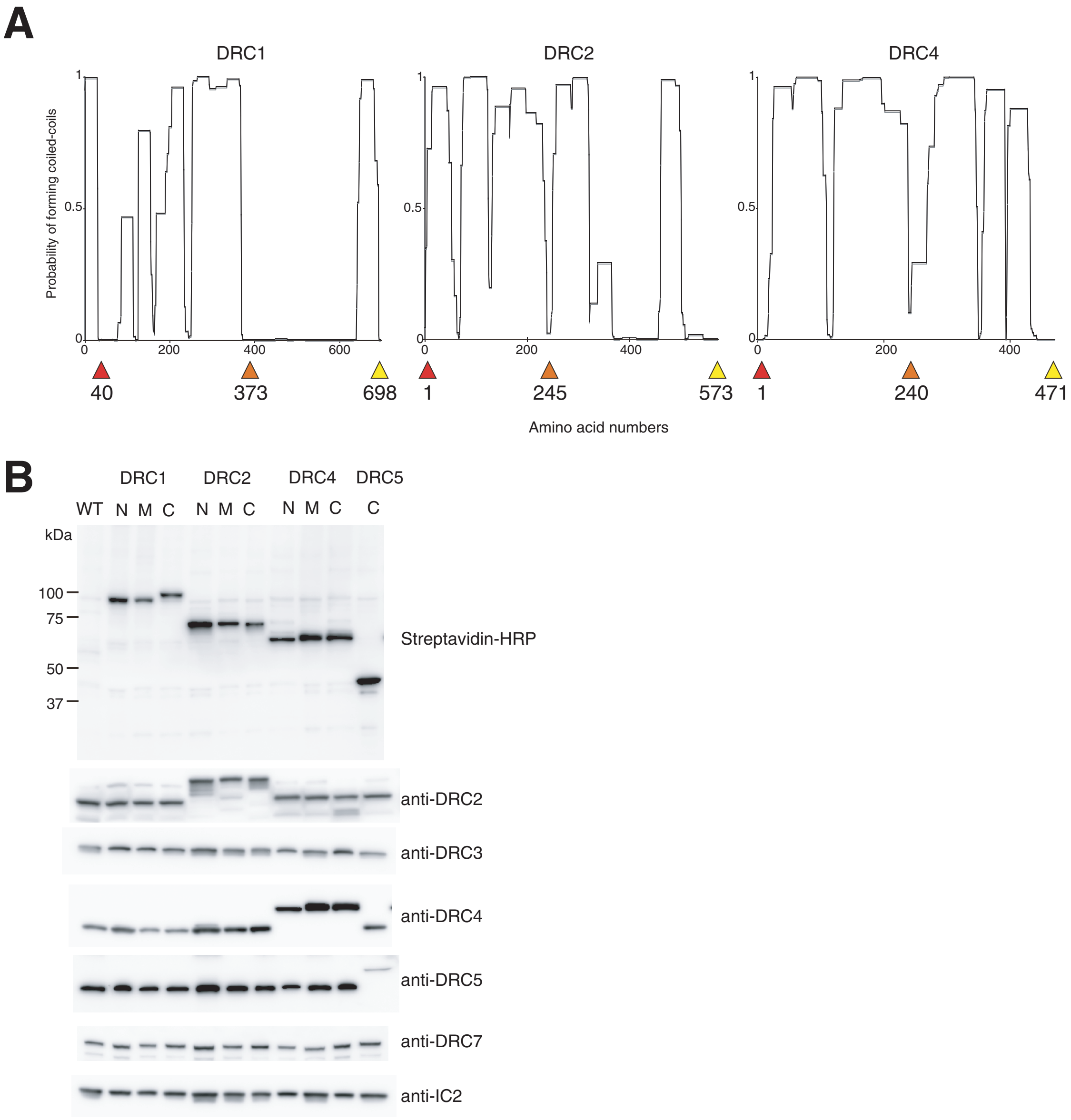

FIGURE 1: BCCP-tagging of N-DRC subunits. (A) Coiled-coil structure prediction using the CoilScan program (Lupas *et al.*, 1991). The probability of coiled-coil formation is plotted along the amino acid sequences. The positions of the inserted BCCP tags are indicated by red (N-terminal), orange (middle), and yellow (C-terminal) arrowheads.
(B) Immunoblots of N-DRC subunits. Axonemal proteins from wild-type (WT) and BCCP-tagged mutant strains were separated with SDS–PAGE and probed with horseradish peroxidase–conjugated streptavidin or the indicated antibodies. N, tagged at the N-terminus; M, tagged in the middle; C, tagged at the C-terminus.

RESULTS

Biotinylation tagging of DRC1, DRC2, and DRC4

To locate the N-DRC subunits with cryo-ET, we added biotin carboxyl carrier protein (BCCP) tags to the amino-terminal (N-terminal), middle, and carboxyl-terminal (C-terminal) segments of DRC1, DRC2, and DRC4 (Figure 1A). To minimize the interference caused by BCCP tagging, we chose the tag positions based on low probability of coiled-coil formation (Lupas *et al.*, 1991). BCCP-tagged DRC1, DRC2, and DRC4 were expressed in the *Chlamydomonas* mutant strains *pf3* (ΔDRC1), *ida6* (ΔDRC2), and *pf2* (ΔDRC4), respectively (Rupp and Porter, 2003; Austin-Tse *et al.*, 2013). The motility defects in these mutants were rescued in the transformed cells (Table 1). Biotinylation of the BCCP-tagged proteins and the presence of other N-DRC subunits were confirmed by immunoblotting (Figure 1B). Fluorescence microscopy showed that Alexa-labeled streptavidin molecules bound the axoneme, suggesting that the BCCP tags on DRC1, DRC2, and DRC4 are accessible by streptavidin (Supplemental Figure S1C).

Structural labeling of DRC1, DRC2, and DRC4

Using cryo-ET and an enhanced streptavidin-labeling method (Oda and Kikkawa, 2013; Oda *et al.*, 2014b), we located DRC1, DRC2, and DRC4 based on the positions of the labeling density (Figure 2 and Supplemental Figure S2). N-DRC is roughly divided into two regions—the “linker” and “base plate” domains, which bind to the B-tubule and A-tubule, respectively (Figure 2A; Heuser *et al.*, 2009). The end of the N-DRC base plate is marked by a hole in the inner junction between the A- and B-tubules (Figure 2A, red arrowhead).

Strain	Abbreviation	Mutated gene	Phenotype	Reference
Wild-type CC-125				
pf3		DRC1	Slow swimming	Huang *et al*. (1982), Wirschell *et al*. (2013)
ida6		DRC2	Slow swimming	Kato *et al*. (1993)
pf2		DRC4	Slow swimming	Huang *et al*. (1982), Rupp and Porter (2003)
sup-pf-4		DRC5	Almost wild type	Huang *et al*. (1982), Bower *et al*. (2013)
oda6		IC2	Slow swimming	Kamiya (1988)
ida7		IC140	Slow swimming	Perrone *et al*. (1998)
pf3-DRC1-N-BCCP	*DRC1N*		Slightly slow	This study
pf3-DRC1-M-BCCP	*DRC1M*		Slightly slow	This study
pf3-DRC1-C-BCCP	*DRC1C*		Slightly slow	This study
ida6-DRC2-N-BCCP	*DRC2N*		Wild type	This study
ida6-DRC2-M-BCCP	*DRC2M*		Wild type	This study
ida6-DRC2-C-BCCP	*DRC2C*		Wild type	This study
pf2-DRC4-N-BCCP	*DRC4M*		Wild type	This study
pf2-DRC4-M-BCCP	*DRC4M*		Wild type	This study
pf2-DRC4-C-BCCP	*DRC4C*		Wild type	This study
ida6-DRC2-C-GFP	*DRC2-GFP*		Wild type	This study
oda6-IC2-C-GFP	*IC2-GFP*		Wild type	This study
ida7-IC140-C-GFP	*IC140-GFP*		Wild type	This study

TABLE 1: **Strains used in this study.**

Of interest, DRC1, DRC2, and DRC4 share almost the same configuration: starting from the linker domain, spanning across the base plate, and ending near the hole on the inner junction. DRC1 appears to be shorter than DRC2 and DRC4, probably because the C-terminal half of DRC1 is not predicted to form a coiled coil (Figure 1A). The labeling density of the N-terminus of DRC4 appeared to be split into two (Figure 2B, bottom), probably because the N-terminal BCCP tag is flipped in two directions. The configuration of DRC1, DRC2, and DRC4 suggests that the three proteins serve as the backbone of N-DRC.

Purification of N-DRC

In a previous report (Bower *et al*., 2013), affinity purification of N-DRC using a hemagglutinin tag did not work well due to high nonspecific binding to the resin. Thus we purified the complex using gel-filtration and ion-exchange chromatography (Figure 3). N-DRC was extracted from the axonemes with 0.4 M NaI (Wirschell *et al*., 2013) and applied to a Superdex 200 10/300 GL column equilibrated with 0.5 M NaCl. N-DRC was eluted near the void volume (Figure 3A). The fractions containing eluted N-DRC were applied to SP Sepharose Fast Flow resin equilibrated with 0.5 M NaCl, and highly purified N-DRC was eluted with 0.7 M NaCl (Figure 3C). The high-salt conditions for binding to and elution from the cation-exchange resin suggest that the surface of the N-DRC is highly positively charged.

The high purity of N-DRC eluted from the cation-exchange resin enabled us to characterize the composition of the complex. Among the 15 bands, we identified DRC2, DRC3, DRC4, DRC5, and DRC7 using immunoblotting (Figure 3, B and C). In agreement with a previous study (Bower *et al*., 2013), peptide mass fingerprinting predicted that seven of the remaining bands were DRC11, DRC1, β-tubulin, DRC9, DRC10, DRC6, and DRC8, in descending order of molecular weight (Figure 3C and Supplemental Table S1). In addition, we detected calmodulin, ubiquitin-like protein, and DRC8 (possibly a degradate) using tandem mass spectrometry (MS/MS) analysis. To confirm this result, we performed immunoblotting using anti-calmodulin antibody used in the previous study to detect calmodulin in the radial spoke (Yang *et al*., 2001). However, the antibody did not bind to the calmodulin candidate in the purified N-DRC (Supplemental Figure S3B). Because calcium-binding proteins show Ca^{2+}-dependent electrophoretic mobility shift (Burgess, 1982; Weber *et al*., 1994), we separated the purified N-DRC by SDS–PAGE in the presence of calcium (Supplemental Figure S3C). The calmodulin-candidate protein showed a clear band shift, which closely resembles that of chicken calmodulin in the previous report (Figure 3 in Weber *et al*., 1994). These results suggest that N-DRC contains calmodulin or at least calcium-binding protein that may be different from what was found in the radial spoke.

We also examined the stoichiometry of N-DRC subunits by measuring the intensity of each band (Figure 3D). The calculated relative amounts of most N-DRC proteins were proportional to the observed molecular weight, suggesting a 1:1 stoichiometry for each subunit. Furthermore, we estimated the number of DRC2 molecules in one N-DRC using green fluorescent protein (GFP) tagging and fluorescence microscopy (Figure 3, E and F; Yanagisawa *et al*., 2014). We expressed GFP-tagged DRC2 in *ida6* and confirmed by immunoblotting that the expression level of DRC2-GFP in the transformed cells was the same as that of DRC2 in wild-type cells (Figure 3E). Next we compared the fluorescence intensity of DRC2-GFP flagella with that of ODA IC2-GFP flagella (Figure 3F and Supplemental Figure S3A). The intensity of DRC2-GFP flagella was about one-fourth of that of IC2-GFP flagella. One ODA contains one IC2 (King and Witman, 1989; King and Kamiya, 2009; King, 2011), and one 96-nm repeat of the DMT has four ODAs and one N-DRC (Goodenough and Heuser, 1985; Heuser *et al*., 2009). Thus one N-DRC is estimated to contain one DRC2 molecule. In addition, we analyzed

IDA *f* IC140-GFP flagella and found that the intensity of IC140-GFP flagella was almost the same as that of DRC2-GFP. Because one IC140 molecule is included in one IDA *f* complex, which repeats every 96 nm (Piperno *et al.*, 1990; King and Kamiya, 2009), this result supports the conclusion of one DRC2 per one N-DRC.

The split labeling densities of DRC4 N-terminus (Figure 2B) raise a possibility that there is more than one DRC4 molecule in intact N-DRC. We examined the stoichiometry of DRC2 and DRC4 using anti-BCCP antibody (Supplemental Figure S3D). Immunoblots showed 1:1 stoichiometry between DRC2 and DRC4, suggesting that there is one DRC4 molecule per one N-DRC.

Structure of 0.4 M NaI–extracted N-DRC

Next we examined the homogeneity of the structure of the purified N-DRC with negative-staining electron microscopy (Figure 4). We observed that the shapes of N-DRC are homogeneous, with a rod-like conformation (Figure 4A). This isolated N-DRC structure is different from that in the axoneme, in which the linker domain is bifurcated (Figure 4B, middle). We speculated that high-salt extraction caused partial disassembly of N-DRC. To test this idea, we observed the N-DRC structure in the axoneme treated with 0.6 M NaCl using cryo-ET (Figure 4B, right). The N-DRC after 0.6 M NaCl treatment appeared to lack the structure indicated by red circles (referred to as the "distal lobe"; Heuser *et al.*, 2009) and the overall rod-like shape resembled the structure of purified N-DRC (Figure 4B, left). On the basis of the structural similarity, we assigned the upper thick region and the lower thin region to the B-tubule binding (linker) and A-tubule binding (base plate) domains, respectively (Heuser *et al.*, 2009).

To verify this polarity assignment, we observed BCCP-tagged N-DRC cross-linked with streptavidin (Figure 4C). In agreement with the assignment, N-DRCs with BCCP tags on the N-termini or C-termini of DRC2

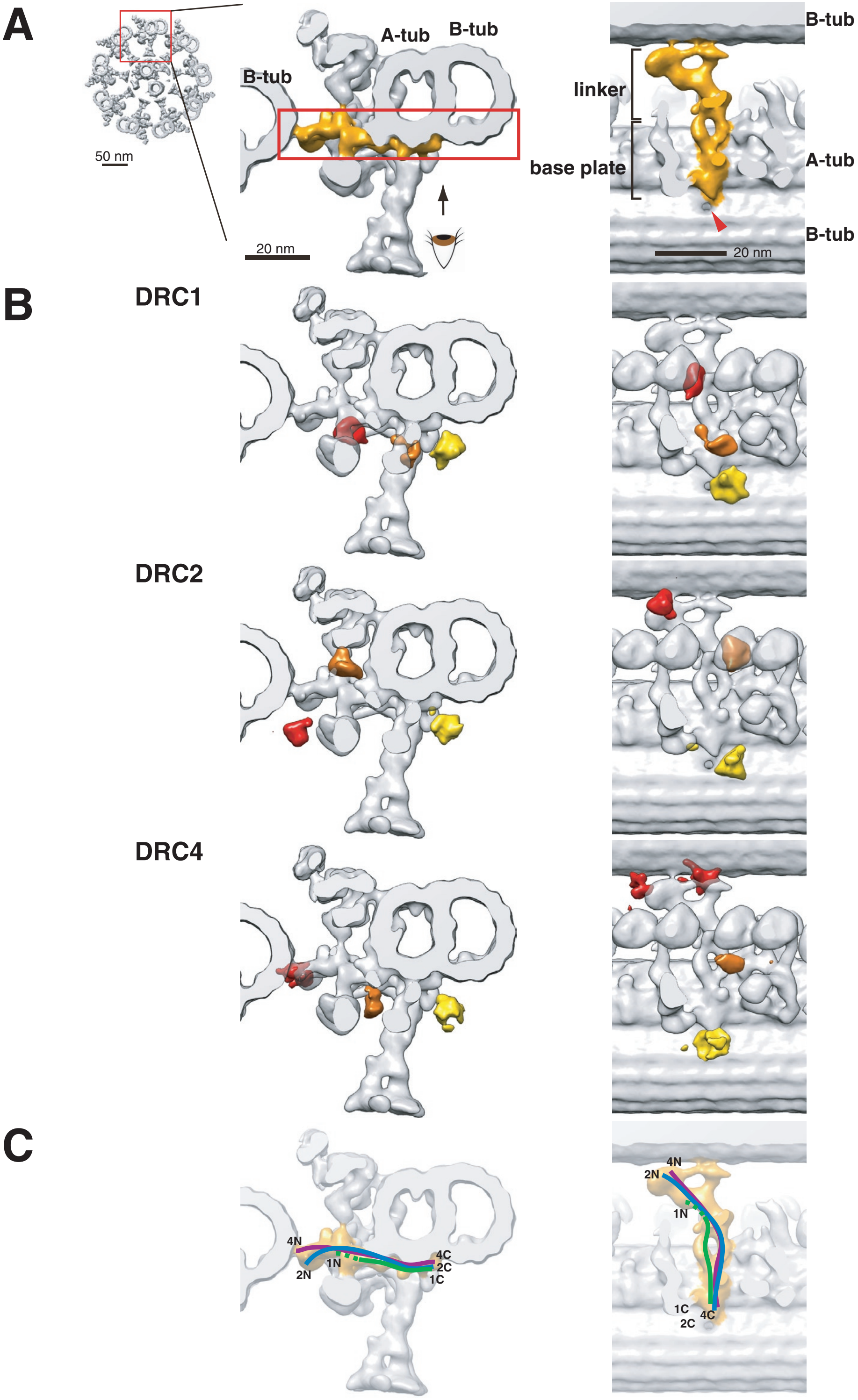

FIGURE 2: Three-dimensional localization of N-DRC subunits using cryo-ET. (A) Three-dimensional localization of N-DRC subunits using cryo-ET structures of N-DRC in *Chlamydomonas* wild-type axoneme. Left, tip-to-base view of the 9+2 structure of the axoneme. Middle, cross-sectional view of the DMT. N-DRC is colored orange. Right, internal view of the boxed region. A-tub, A-tubule; B-tub, B-tubule. The B-tubule–binding and A-tubule–binding regions of N-DRC are referred to as the linker and base plate, respectively (Heuser *et al.*, 2009). (B) Structural labeling of N-DRC. DRC1, DRC2, and DRC4 were tagged with BCCP and labeled with streptavidin and biotinylated cytochrome *c*. The positions of the enhanced streptavidin labels were visualized by comparing the averaged subtomograms of the wild-type DMT (gray) with those of the labeled DMTs. The colored regions indicate the signals of the streptavidin-labels. Red, N-terminal; orange, middle segment; and yellow, C-terminal tags. (C) A model of N-DRC architecture. Possible locations of DRC1, DRC2, and DRC4 are shown with green, blue, and violet lines, respectively. N and C indicate N- and C-termini of the proteins, respectively. 1, 2, and 4 correspond to DRC1, DRC2, and DRC4, respectively. The broken line at the N-terminal regions of DRC1 indicates ambiguity in localization, as the BCCP tag added to the N-terminal segment of DRC1 was 40 amino acids away from the N-terminus.

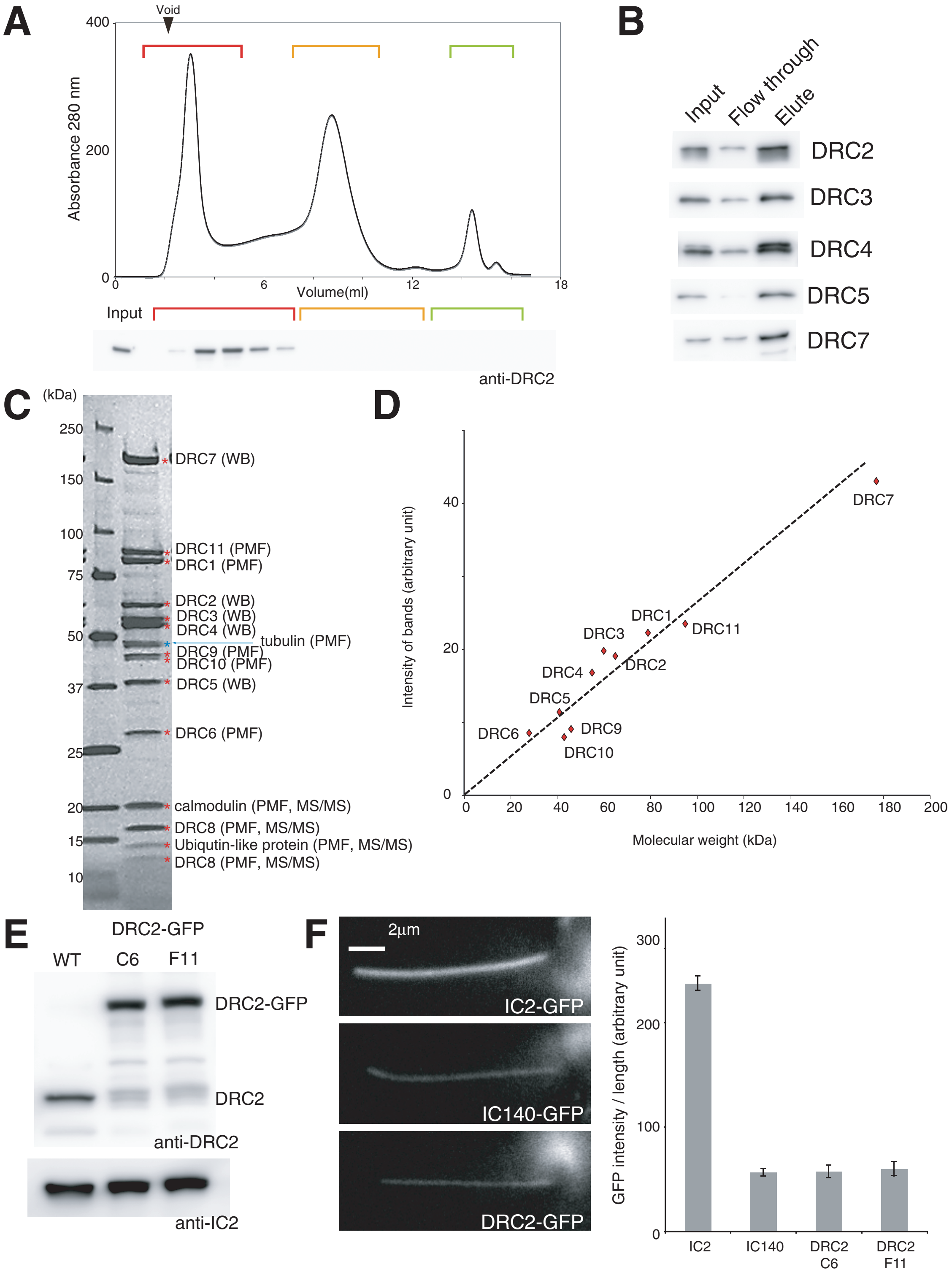

FIGURE 3: Purification of N-DRC. (A) Gel-filtration chromatography of the 0.4 M NaI extract from the wild-type axoneme. The extract was fractionated using a Superdex 200 10/300 GL column equilibrated with 0.5 M NaCl buffer. Immunoblotting using anti-DRC2 antibody indicates that the first peak near the void volume contains N-DRC. (B) Fractionation of N-DRC with ion-exchange chromatography. Fractions from the gel-filtration column containing N-DRC were applied to SP Sepharose Fast Flow cation-exchange resin, and the bound proteins were eluted with 0.7 M NaCl buffer. Immunoblotting showed that N-DRC subunits remained attached to the resin in the presence of 0.5 M NaCl and were eluted with 0.7 M NaCl. (C) SDS–PAGE of the 0.7 M elutate from the cation-exchange resin. The gel was stained with Oriole Fluorescent Gel Stain (Bio-Rad). Among the 15 clear bands observed, we identified 5 using Western blotting and predicted the rest of the bands using peptide mass fingerprinting (PMF) and/or MS/MS analysis. (D) Stoichiometry estimation of N-DRC subunits. A linear relationship exists between the band intensity and the molecular weight of each protein, suggesting a 1:1 stoichiometry. The values were calculated from five independent

were connected between the thick linkers or between the thin base plates, respectively. These results suggest that N-DRC extracted with 0.4 M NaI lacks the distal lobe region.

Effect of N-DRC on the microtubule-sliding activity of ODA

To examine the microtubule-binding properties of N-DRC, we performed in vitro motility assays (Figure 5). We fixed the BCCP-tagged ODA and N-DRC on a glass slide via biotin–bovine serum albumin (BSA) and streptavidin (Figure 5A; Furuta *et al.*, 2009). In the absence of ODA, microtubules bound to N-DRC–coated glass slides regardless of the positions of the BCCP tags, suggesting that both the linker and base plate of purified N-DRC can bind to microtubules. Next we measured the speed of microtubule sliding in the presence of a constant amount of ODA and various amounts of N-DRC (Figure 5, C and D). We controlled the amount of N-DRC bound to streptavidin by adding biocytin (biotinyl-L-lysine) and quantified amounts of ODA and N-DRC on the glass slide using immunoblotting (Figure 5C). ODA-driven microtubule sliding speed was reduced by ~20% ($p < 0.2\%$, $n = 10$) in the presence of N-DRC. Of interest, microtubule sliding was observed even in the presence of fourfold molar excess of N-DRC. The inhibitory effect of N-DRC on ODA motility was relatively higher when N-DRC was anchored at the base plate side (DRC2C, red) than when anchored at the linker side (DRC2N, black; Figure 5D). Given that the physiological molar ratio of ODA to N-DRC in the axoneme is 4:1 (Heuser *et al.*, 2009), our result suggests that microtubule cross-bridging by N-DRC imposes a load on ODA in flagella, but the load is small enough to allow microtubule sliding.

DISCUSSION

In this study, we used the biotin-streptavidin structural labeling method (Oda and Kikkawa, 2013; Oda *et al.*, 2014b) to obtain more precise structural information of N-DRC subunits than the previous report (Heuser *et al.*, 2009). Using this method, we can accurately locate proteins based on the positions of the streptavidin labels bound to the biotin-tagged target proteins. The results of the structural labeling of DRC1, DRC2, and DRC4 indicate that the core of N-DRC is made of bundled coiled-coil proteins rather than clustering of globular proteins. We also successfully labeled the C-terminus of DRC5 and identified the position in the middle of the N-DRC (Supplemental Figure S4A). However, we could not detect Alexa–streptavidin binding to the DRC5-N-BCCP axoneme, probably because the N-terminus of DRC5 may be buried deep in the structure. We tried different insertion positions and longer linkers, but none was successful. DRC5-C-BCCP immunoblotting (Figure 1B) showed low expression of BCCP-tagged DRC5, indicating that the addition of BCCP interferes with the incorporation of DRC5 into N-DRC. Although structural labeling using the BCCP tag is a powerful method, different approaches may be necessary to locate complex subunits that are not adequately exposed to the surface.

Unfortunately, N-DRC extracted with 0.4 M NaI was not intact (Figure 4). Although we characterized the subunit composition and microtubule-binding properties of purified N-DRC, isolating intact N-DRC will be necessary for drawing confident conclusions. The difference in extraction conditions (0.6 M NaCl vs. 0.4 M NaI) suggests that the distal lobe loosely attaches to N-DRC, whereas the base plate is tightly bound to the DMT. Thus finding a condition in which intact N-DRC can be extracted from the axoneme in a single step will be extremely difficult. One possible solution is to pull down the components of the distal lobe using partial N-DRC as bait. For determining the purification conditions of intact N-DRC, note that N-DRC is highly unstable in low-salt conditions (<150 mM NaCl), and aggregates were observed under a dark-field microscope when we reduced the salt concentration in the presence of N-DRC that was not bound to the glass surface.

Dynein-driven DMT sliding is believed to be converted into the bending motion of the axoneme by the nexin links (Summers and Gibbons, 1971; Warner, 1976). Two models have been proposed to explain the inter-DMT elasticity: the detach–reattach model (Minoura *et al.*, 1999) and the fixed-spring model (Lindemann *et al.*, 2005). The first model suggests that the nexin links translocate along the DMT by cooperative detachment from and attachment to the B-tubule. The second model suggests that the nexin links are permanently fixed between the DMTs and stretch in response to the DMT sliding, for example, by protein unfolding. If the second model is correct, the ODA-driven microtubule sliding should be slowed down and eventually halted as the microtubule translocates in the presence of N-DRC because the N-DRC has a finite length. However, the microtubule sliding speeds took constant values for >3 s and 5-µm length regardless of the presence of N-DRC in our experiments, suggesting that N-DRC can temporarily detach from the microtubules and allow continuous sliding. Our cryo-ET result that a bundle of coiled-coil domains forms the backbone of N-DRC also favors the first model because simultaneous unfolding of three coiled-coil proteins is unlikely. However, our results are not sufficient to justify the detach–reattach model because the purified N-DRC appeared to lack half of the B-tubule–binding regions. Performing the same microtubule-sliding assays using intact N-DRC will be necessary.

MATERIALS AND METHODS

Strains and reagents

Chlamydomonas reinhardtii strains 137c cells were grown in Tris-acetate-phosphate (TAP) medium. To screen transformants, cells were grown on TAP agar supplemented with paromomycin (10 µg/ml; Sigma-Aldrich, St. Louis, MO). *C. reinhardtii* strains used for this study are listed in Table 1.

Antibodies

The cDNA sequences encoding the full-length proteins of DRC3 and DRC5 were inserted into pET24a, and the polypeptides were expressed in *Escherichia coli* cells. Anti-DRC3 and anti-DRC5 rabbit polyclonal antibodies were raised against the purified proteins. The cDNA sequence encoding amino acids 141–228 of *Chlamydomonas* acetyl-CoA carboxylase BCCP was inserted into pGEX-6p-2 plasmid, and the polypeptides were expressed in *E. coli* cells. Anti-BCCP rabbit polyclonal antibody was raised against the purified proteins. Antibodies used in this study are summarized in Table 2.

measurements. (E, F) Quantification of GFP fluorescence in DRC2-GFP flagella. (E) DRC2-GFP was expressed in *ida6* mutant cells, and the wild-type expression levels of the protein in two transformants were confirmed with immunoblotting. Similarly, the wild-type expression levels of IC2-GFP and IC140-GFP were observed (Supplemental Figure S3). (F) Estimation of the number of DRC2 molecules in N-DRC. Live cells expressing IC2-GFP, IC140-GFP, and DRC2-GFP were attached to the glass slide, and the GFP fluorescence of the flagella was measured and divided by the length. The intensity of IC2-GFP was about four times stronger than that of IC140-GFP and DRC2-GFP, suggesting that one DRC2 molecule exists per 96 nm along the DMT. Mean ± SEM were calculated from 10 measurements.

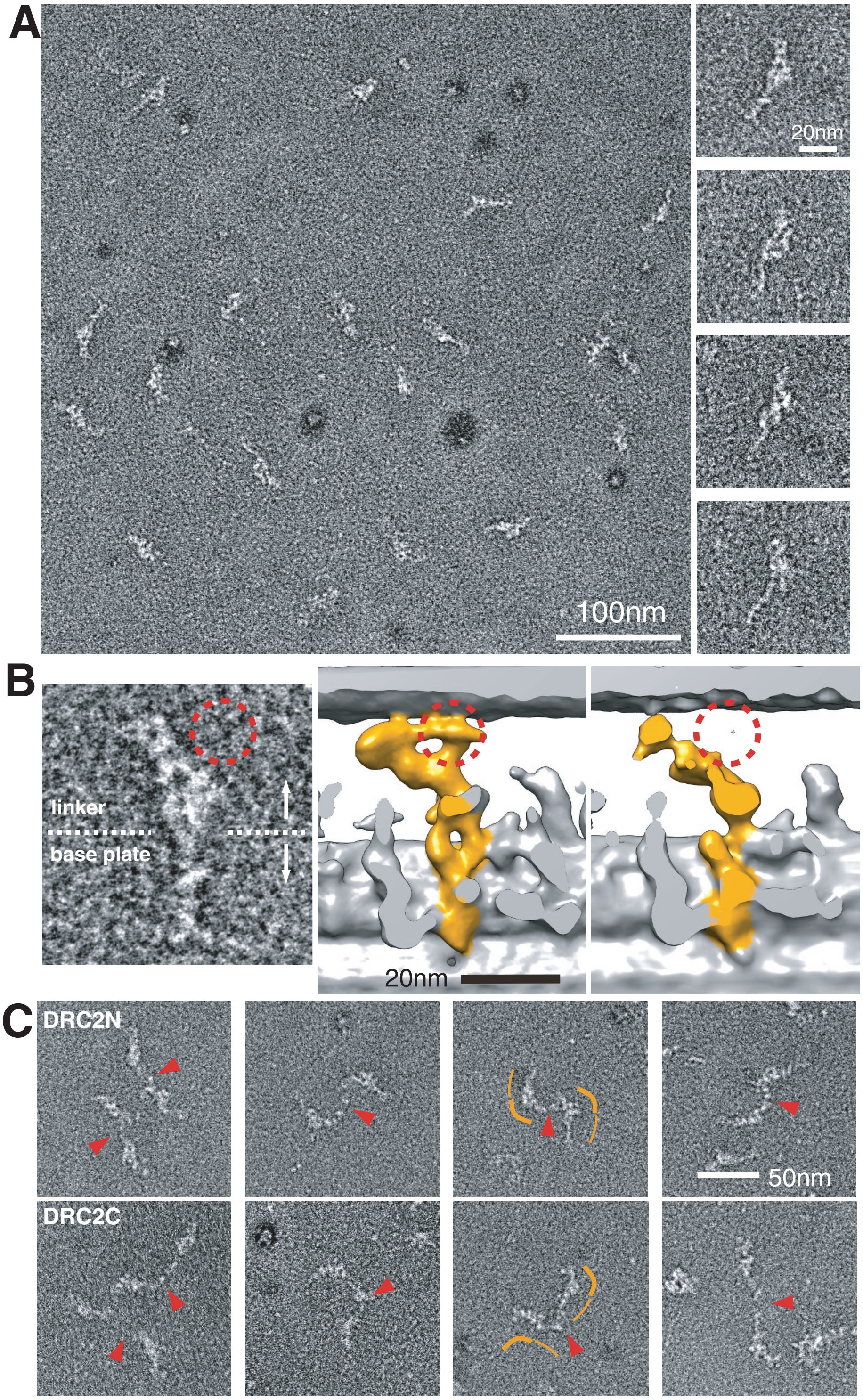

FIGURE 4: Negative-staining electron microscopy of purified N-DRC. (A) Negative-staining images of N-DRC purified from 0.4 M NaI extracts. N-DRC molecules were adsorbed onto a carbon grid and stained with uranyl acetate. Nearly homogeneous slender, rod-shape molecules are seen. Left, typical views of N-DRC. (B) Comparison between a negative-stained image of purified N-DRC and cryo-ET images of intact and 0.6 M NaCl–treated N-DRC. Judging from the structural similarity, the thick and thin regions of purified N-DRC correspond to the linker and base plate, respectively. Red circles indicate that the distal half of the B-tubule–binding region, referred to as the "distal lobe" in Heuser *et al.* (2009), was missing in purified and 0.6 M NaCl–treated N-DRC. (C) Cross-linking of BCCP-tagged N-DRC with streptavidin. N-DRC purified from *DRC2N* and *DRC2C* axonemes was incubated with streptavidin and adsorbed onto carbon grids. Cross-linked N-DRC was seen in the negative-stained images. Red arrowheads indicate the expected positions of the cross-linking streptavidin. Thick and thin orange curves indicate the orientation of the cross-linked N-DRC. N-DRC with BCCP tags on the linker side (DRC2N) and base-plate side (DRC2C) was cross-linked between the thick regions and between the thin regions, respectively.

Construction of FAP59 and FAP172 expression vectors

Fragments spanning from 1000 base pairs upstream of the noncoding sequence to immediately before the stop codon for the genes encoding DRC2, DRC4, and DRC5 were amplified with genomic PCR using genomic DNA from the wild-type strain CC-125 and then inserted into a custom *Chlamydomonas* expression plasmid containing the 3′ untranslated region of the LC8 (FLA14) gene followed by a paromomycin-resistance cassette (Yanagisawa *et al.*, 2014). For biotinylation tagging of the N- or C-terminus, the tag sequence corresponding to amino acids 141–228 of *Chlamydomonas* acetyl-CoA carboxylase BCCP was fused immediately before the start or stop codon of the genes using an In-Fusion HD Cloning Kit (Clontech Laboratories, Mountain View, CA). For DRC1, the full-length cDNA sequence was amplified with reverse transcription-PCR using cDNA from CC-125 and then inserted into pIC2-N-BCCP and pIC2-C-BCCP plasmids (Supplemental Figure S1A). However, because we could not detect streptavidin binding to the BCCP added to the N-terminus of DRC1, we inserted the BCCP sequence between Glu-40 and Asn-41 of DRC1. For BCCP tagging in the middle segment of the sequences, the tag sequence was fused immediately after the codon encoding Lys-373 of DRC1, His-245 of DRC2, and Thr-240 of DRC4.

Preparation of axonemes

Chlamydomonas cells were deflagellated with dibucaine-HCl (Wako Pure Chemical Industries, Tokyo, Japan), and axonemes were collected with centrifugation (Piperno *et al.*, 1977). Flagella were demembranated with 1% Nonidet P-40 in HMDENa buffer or HMDEK buffer composed of 30 mM 4-(2-hydroxyethyl)-1-piperazineethanesulfonic acid–NaOH, pH 7.2, 5 mM $MgCl_2$, 1 mM dithiothreitol, 1 mM ethylene glycol tetraacetic acid, 50 mM NaCl or 50 mM CH_3COOK, and 1× protease inhibitor cocktail (Nacalai Tesque, Kyoto, Japan).

Electrophoresis and immunoblotting

Axonemal proteins were resolved with SDS–PAGE on 5–20% polyacrylamide gradient gels (Nacalai Tesque) and blotted onto polyvinylidene difluoride membranes, which were fixed with 0.5% glutaraldehyde for

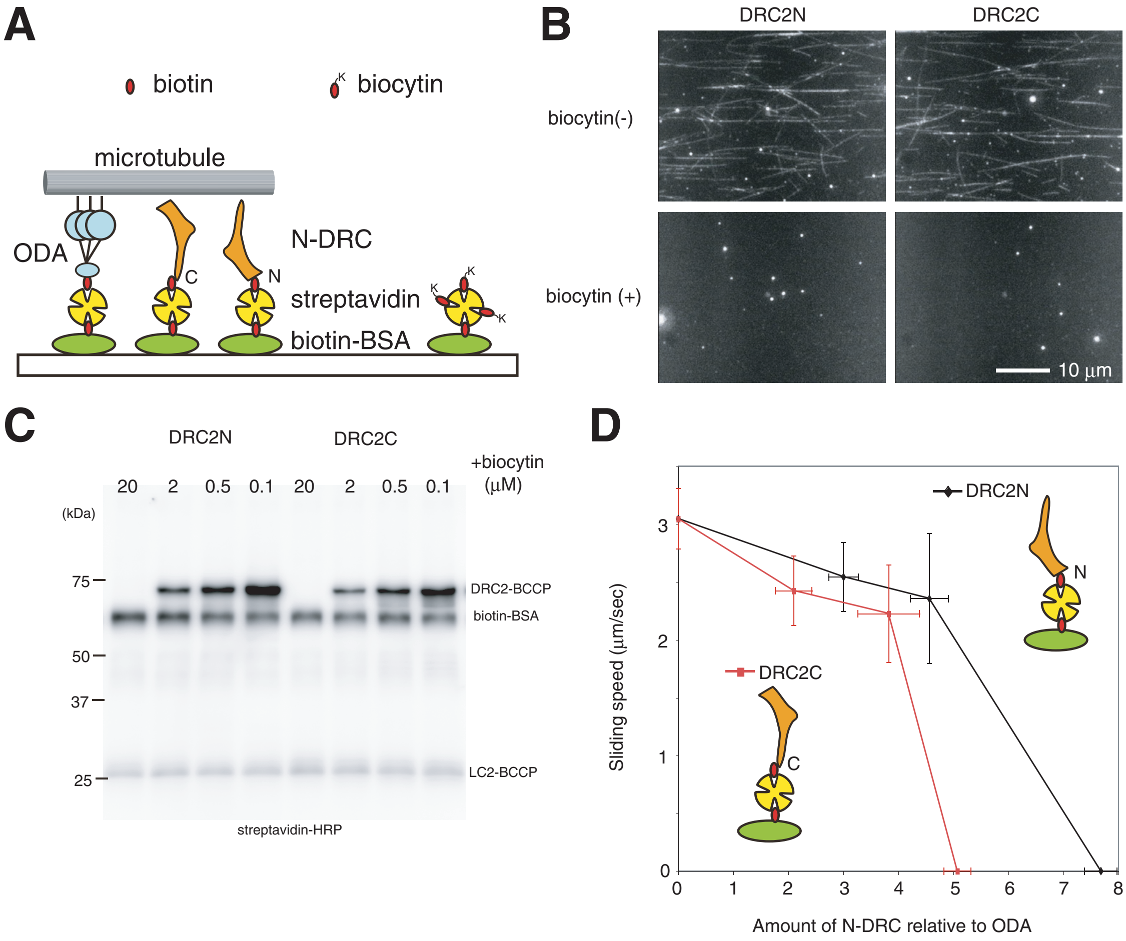

FIGURE 5: Microtubule-sliding assay in the presence of ODA and N-DRC. (A) Schematic picture of the microtubule-sliding assay system. BCCP-tagged ODA and N-DRC were fixed on the glass slide via biotin-BSA and streptavidin. Orientation of N-DRC relative to the microtubule is expected to be dependent on the position of the BCCP tag. N-DRC with DRC2N or DRC2C is likely to interact with the microtubule through the A-tubule–binding (base plate) side or the B-tubule–binding (linker) side, respectively. (B) N-DRC binds to microtubules. Purified N-DRC with DRC2-N-BCCP or DRC2-C-BCCP was applied to a streptavidin-coated flow chamber with or without 0.1 mM biocytin, followed by addition of microtubules. In the absence of biocytin, N-DRC was adsorbed onto the glass surface and captured microtubules. In the presence of biocytin, biotin-binding sites of streptavidin were blocked, and no microtubules were observed on the glass surface. We observed no significant difference in the microtubule-binding capacity between N-DRCs in the two different orientations. Addition of ATP did not release microtubules from the glass slides. (C, D) Effect of N-DRC on ODA-driven microtubule sliding. (C) After adsorption of ODA onto the streptavidin-coated glass slide, N-DRC was applied to the flow chamber along with different concentrations of biocytin. The proteins that bound to the glass surface were retrieved by washing the flow chamber with SDS sample buffer and separated with SDS–PAGE. The relative amounts of ODA and N-DRC in the chamber were quantified using streptavidin–horseradish peroxidase blotting. (D) The microtubule sliding speeds were plotted against the amount of N-DRC relative to ODA. N-DRC did not block ODA-driven microtubule sliding up to fourfold molar excess. Mean ± SEM were calculated from 10 measurements.

10 min and probed with streptavidin conjugated to horseradish peroxidase (Thermo Scientific, Rockford, IL) or the indicated primary antibodies. For gel staining, the polyacrylamide gradient gels were stained with Oriole Fluorescent Gel Stain (Bio-Rad, Hercules, CA). For silver staining of the purified N-DRC (Supplemental Figure S3C), we fixed the gel with or without 10% glutaraldehyde following the method described in Schleicher and Watterson (1983).

Fluorescence microscopy detection of axonemes

Demembranated axonemes were attached to glass slides and blocked with 1 mg/ml BSA in HMDEK buffer. Axonemes were incubated with 1 µg/ml Alexa Fluor 546–conjugated streptavidin (Invitrogen, Carlsbad, CA) for 1 min. Labeled axonemes were washed three times with HMDEK buffer and observed using a fluorescence microscope (IX70; Olympus, Tokyo, Japan). Images were recorded using a charge-coupled device camera (ORCA-R2; Hamamatsu Photonics, Hamamatsu, Japan).

To quantify GFP fluorescence signals, live cells with flagella attached to a glass slide were observed using an IX70 microscope, and images were recorded using an ORCA-R2 camera. Fluorescence intensities of flagella were measured using ImageJ (National Institutes of Health, Bethesda, MD).

Antibody (clone #)	Host	Dilution (Western blotting)	Reference or source
Anti-IC2 (1869A)	Mouse	1:10,000	D6168 (Sigma-Aldrich)
Anti-IC140	Rabbit	1:5000	Oda *et al*. (2014a)
Anti-DRC2	Rabbit	1:5000	Oda *et al*. (2013)
Anti-DRC4	Rabbit	1:5000	Oda *et al*. (2013)
Anti- DRC7	Rabbit	1:5000	Oda *et al*. (2013)
Anti-DRC3	Rabbit	1:5000	This study
Anti-DRC5	Rabbit	1:5000	This study
Anti-BCCP	Rabbit	1:10,000	This study
Anti-calmodulin	Mouse	1:1000	Ab-1 2D1 (Abcam, Cambridge, UK)

TABLE 2: Antibodies used in this study.

Sample preparation for cryo-ET

Streptavidin–cytochrome *c* labeling of BCCP-tagged axonemes was carried out as described (Oda *et al*., 2014b). In brief, demembranated axonemes were incubated with 0.05 mg/ml streptavidin for 15 min at 4°C in HMDEK buffer. The axonemes were then washed with HMDEK buffer and incubated with 0.05 mg/ml biotinylated cytochrome *c* for 15 min at 4°C in the presence of 1 mg/ml BSA. Next the axonemes were washed and again incubated with streptavidin. Incubation with cytochrome *c* and streptavidin was repeated once if necessary. Labeled or unlabeled axonemes were resuspended in HMDEK buffer at a concentration of 0.02 mg/ml and mixed with an equal amount of 15-nm colloidal gold suspension conjugated with BSA (Aurion, Wageningen, Netherlands). Home-made holey carbon grids were glow discharged for 20 s. Suspended axonemes plus colloidal gold (5 µl) were loaded onto the grids and plunge-frozen in liquid ethane at −180°C with a Leica EM GP automated plunge-freezing device (Leica Microsystems, Wetzlar, Germany).

Image acquisition

Grids were transferred to a JEM-3100FEF transmission electron microscope (JEOL, Tokyo, Japan) with a Gatan 914 high-tilt liquid nitrogen cryo-transfer holder (Gatan, Pleasanton, CA). Tilt series images were recorded at −180°C using a TemCam-F416 CMOS camera (TVIPS, Gauting, Germany), and automated acquisition was performed using Recorder software (System in Frontier, Tokyo, Japan). The angular range of the tilt series was from −65 to 65° with 2.0° increments. The total electron dose was limited to ~100 $e^-/Å^2$. Images were recorded at 300 keV, with 6- to 7-µm defocus, at a magnification of 25,700× and a pixel size of 6 Å. An in-column omega energy filter was used to enhance image contrast in the zero-loss mode with a slit width of 20 eV.

Image processing

Image processing for subtomogram averaging of DMT structures was carried out as described, with minor modifications (Oda and Kikkawa, 2013; Oda *et al*., 2014b). Tilt series images were aligned and backprojected to reconstruct 3D tomograms using the IMOD software package (Kremer *et al*., 1996). Tomograms of intact axonemes with a high signal-to-noise ratio were selected and used for subtomogram averaging of the 96-nm repeats of DMTs. Alignment and averaging of subtomograms were conducted using custom Ruby-Helix scripts (Metlagel *et al*., 2007) and the PEET software suite (Nicastro *et al*., 2006). The numbers of DMT subtomograms averaged were as follows: 650 for wild type, 635 for DRC1N, 664 for DRC1M, 896 for DRC1C, 702 for DRC2N, 950 for DRC2M, 872 for DRC2C, 712 for DRC4N, 680 for DRC4M, and 912 for DRC4C. The effective resolutions determined with Fourier shell correlation with a cutoff value of 0.5 were as follows: 4.5 nm for wild type, 4.9 nm for DRC1N, 4.3 nm for DRC1M, 4.3 nm for DRC1C, 4.3 nm for DRC2N, 4.5 nm for DRC2M, 4.4 nm for DRC2C, 4.5 nm for DRC4N, 4.6 nm for DRC4M, 4.3 nm for DRC4C, and 4.5 nm for DRC5C (Supplemental Figure S4B).

Surface renderings were generated using UCSF Chimera (Pettersen *et al*., 2004). The electron microscopy maps of averaged DMT are available at the EM Data Bank (www.emdatabank.org) under the accession numbers EMD-6154–6164.

Statistical analysis

To identify statistically significant differences, we applied a Student's *t* test to compare wild-type and streptavidin-labeled axonemes as described previously (Oda and Kikkawa, 2013; Oda *et al*., 2014b). First, wild-type and streptavidin-labeled subtomograms were randomly divided into three data sets. Subtomograms for each data set were aligned and averaged, and a total of six averaged subtomograms was created. We calculated the *t* value for each voxel and presented it as a single *t*-value map. The isosurface threshold values were $t > 7.17$, with a one-tailed probability of <0.1%.

Purification of N-DRC

Axonemes were washed once with HMDE buffer plus 0.6 M NaCl and twice with HMDE buffer plus 0.2 M NaI. Washed axonemes were incubated in HMDE buffer plus 0.4 M NaCl on ice for 30 min and centrifuged at 22,000 × *g* for 10 min. The supernatant were fractionated with gel-filtration chromatography using a Superdex 200 10/300 GL column (GE Healthcare Life Science, Pittsburgh, PA) equilibrated with HMDE plus 0.5 M NaCl. Fractions containing N-DRC were identified using immunoblots and applied to a 50-µl bed volume of SP Sepharose Fast Flow resin (GE Healthcare Life Science). The resin was washed three times with HMDE buffer plus 0.5 M NaCl, and N-DRC was eluted with HMDE buffer plus 0.7 M NaCl. The gel-filtration step can be replaced with overnight dialysis against HMDE buffer plus 0.5 M NaCl without changing the composition of the final eluate.

Mass spectroscopic analysis

Purified N-DRC was separated with SDS–PAGE, and the bands were excised from Oriole-stained gel. The gel slices were digested with trypsin (Promega, Madison, WI) and subjected to peptide-mass fingerprinting analysis using matrix-assisted laser desorption/ionization–time-of-flight (TOF) mass spectrometry (Microflex LRF 20; Bruker Daltonics, Bremen, Germany) and the MASCOT search program (Matrix Science, Boston, MA). For the MS/MS analysis, samples were analyzed using the Applied Biosystems 4700 proteomics analyzer with TOF/TOF ion optics. MS/MS mode was operated with 1-keV collision energy; air was used as the collision gas, such that nominally single collision conditions were achieved. Sequence tag searches were performed with the program MASCOT.

Negative staining of purified N-DRC

Purified N-DRC in HMDE buffer plus 0.7 M NaCl was diluted to 1 µg/ml with the same buffer and adsorbed onto glow-discharged carbon grids, which were stained three times with 2% (wt/vol) uranyl acetate. Images were recorded using a JEM-3100FEF microscope and a TemCam-F416 camera, with 3- to 4-µm defocus, at a magnification of 73,700× and a pixel size of 1.9 Å.

Microtubule-sliding assay

BCCP-tagged ODA αβγ particles were purified from *LC2-BCCP-oda12* flagella with ion-exchange chromatography on an UnoQ column (Bio-Rad; Furuta *et al*., 2009). A flow chamber (volume, ~10 µl), composed of a glass slide and a coverslip with two slivers of double-sided adhesive tape as spacers, was sequentially coated with 1 mg/ml biotinamidocaproyl BSA (Sigma-Aldrich) and 0.1 mg/ml streptavidin (Wako Pure Chemicals) and blocked with 1 mg/ml BSA in HMDE buffer. Purified BCCP-tagged ODA particles (0.1 mg/ml) were applied to the flow chamber and adsorbed onto the glass surface via biotin-streptavidin binding for 3 min. Unbound ODA particles were washed with HMDE buffer plus 0.7 M NaCl and 1 mg/ml BSA, and 10 µg/ml BCCP-tagged N-DRC with various concentrations of biocytin (Thermo Scientific) in HMDE buffer plus 0.7 M NaCl was applied to the flow chamber. The biotinylated molecules were allowed to bind to the remaining biotin binding sites of streptavidin for 5 min. Unbound molecules were washed three times with HMDE plus 0.7 M NaCl and another three times with HMDE plus 1 mg/ml BSA and 10 µM paclitaxel (Wako Pure Chemicals). Taxol-stabilized microtubules in HMDE buffer plus 10 µM paclitaxel were applied to the flow chamber, and sliding of the microtubules was initiated by adding 1 mM ATP in HMDEK plus 10 µM paclitaxel. Sliding of microtubules was observed using a dark-field microscope (BX53; Olympus) equipped with a 100-W mercury lamp, and images were recorded with an electron- multiplying charge-coupled device (ADT-33S; FLOVEL, Tokyo, Japan). After recording, the flow chamber was washed twice with HMDE buffer plus 0.7 M NaCl and twice with HMDE buffer. The proteins bound to the glass slide were recovered by washing the chamber with SDS sample buffer (20 mM Tris-HCl, pH 6.8, 2% SDS, 0.2% bromophenol blue, 10% glycerol, and 100 mM dithiothreitol).

ACKNOWLEDGMENTS

We thank Toshiki Yagi (Prefectural University of Hiroshima, Hiroshima, Japan) for technical assistance and valuable advice. This work was supported by the Japan Science and Technology Agency (CREST, to M.K.), the Kazato Research Foundation (to T.O.), and the Takeda Science Foundation (to M.K. and T.O.).

REFERENCES

Austin-Tse C, Halbritter J, Zariwala MA, Gilberti RM, Gee HY, Hellman N, Pathak N, Liu Y, Panizzi JR, Patel-King RS, *et al.* (2013). Zebrafish ciliopathy screen plus human mutational analysis identifies C21orf59 and CCDC65 defects as causing primary ciliary dyskinesia. Am J Hum Genet 93, 672–686.

Badano JL, Mitsuma N, Beales PL, Katsanis N (2006). The ciliopathies: an emerging class of human genetic disorders. Annu Rev Genomics Hum Genet 7, 125–148.

Bower R, Tritschler D, Vanderwaal K, Perrone CA, Mueller J, Fox L, Sale WS, Porter ME (2013). The N-DRC forms a conserved biochemical complex that maintains outer doublet alignment and limits microtubule sliding in motile axonemes. Mol Biol Cell 24, 1134–1152.

Burgess WH (1982). Characterization of calmodulin and calmodulin isotypes from sea urchin gametes. J Biol Chem 257, 1800–1804.

Drummond IA (2012). Cilia functions in development. Curr Opin Cell Biol 24, 24–30.

Fliegauf M, Benzing T, Omran H (2007). When cilia go bad: cilia defects and ciliopathies. Nat Rev Mol Cell Biol 8, 880–893.

Furuta A, Yagi T, Yanagisawa HA, Higuchi H, Kamiya R (2009). Systematic comparison of in vitro motile properties between Chlamydomonas wild-type and mutant outer arm dyneins each lacking one of the three heavy chains. J Biol Chem 284, 5927–5935.

Gardner LC, O'Toole E, Perrone CA, Giddings T, Porter ME (1994). Components of a "dynein regulatory complex" are located at the junction between the radial spokes and the dynein arms in Chlamydomonas flagella. J Cell Biol 127, 1311–1325.

Goodenough UW, Heuser JE (1985). Outer and inner dynein arms of cilia and flagella. Cell 41, 341–342.

Haimo LT, Rosenbaum JL (1981). Cilia, flagella, and microtubules. J Cell Biol 91, 125s–130s.

Heuser T, Raytchev M, Krell J, Porter ME, Nicastro D (2009). The dynein regulatory complex is the nexin link and a major regulatory node in cilia and flagella. J Cell Biol 187, 921–933.

Huang B, Ramanis Z, Luck DJ (1982). Suppressor mutations in Chlamydomonas reveal a regulatory mechanism for Flagellar function. Cell 28, 115–124.

Kamiya R (1988). Mutations at twelve independent loci result in absence of outer dynein arms in Chylamydomonas reinhardtii. J Cell Biol 107, 2253–2258.

Kato T, Kagami O, Yagi T, Kamiya R (1993). Isolation of two species of Chlamydomonas reinhardtii flagellar mutants, ida5 and ida6, that lack a newly identified heavy chain of the inner dynein arm. Cell Struct Funct 18, 371–377.

Kikkawa M (2013). Big steps toward understanding dynein. J Cell Biol 202, 15–23.

King SM (2011). Composition and assembly of axonemal dyneins. In: Dyneins: Structure, Biology and Disease, ed. SM King, Boston: Academic Press, 208–243.

King SM, Kamiya R (2009). Axonemal dyneins: assembly, structure, and force generation. In: The Chlamydomonas Sourcebook, Vol. 3, 2nd ed., ed. GB Witman, Oxford, UK: Academic Press, 144–145.

King SM, Witman GB (1989). Molecular structure of Chlamydomonas outer arm dynein. In: Cell Movements, Vol. 1: The Dynein ATPases, ed. FD Warner, P Satir, and IR Gibbons, New York: Alan R. Liss, 61–75.

Kremer JR, Mastronarde DN, McIntosh JR (1996). Computer visualization of three-dimensional image data using IMOD. J Struct Biol 116, 71–76.

Lin J, Tritschler D, Song K, Barber CF, Cobb JS, Porter ME, Nicastro D (2011). Building blocks of the nexin-dynein regulatory complex in Chlamydomonas flagella. J Biol Chem 286, 29175–29191.

Lindemann CB, Macauley LJ, Lesich KA (2005). The counterbend phenomenon in dynein-disabled rat sperm flagella and what it reveals about the interdoublet elasticity. Biophys J 89, 1165–1174.

Lupas A, Van, Dyke M, Stock J (1991). Predicting coiled coils from protein sequences. Science 252, 1162–1164.

Metlagel Z, Kikkawa YS, Kikkawa M (2007). Ruby-Helix: an implementation of helical image processing based on object-oriented scripting language. J Struct Biol 157, 95–105.

Minoura I, Yagi T, Kamiya R (1999). Direct measurement of inter-doublet elasticity in flagellar axonemes. Cell Struct Funct 24, 27–33.

Nicastro D, Schwartz C, Pierson J, Gaudette R, Porter ME, McIntosh JR (2006). The molecular architecture of axonemes revealed by cryoelectron tomography. Science 313, 944–948.

Oda T, Kikkawa M (2013). Novel structural labeling method using cryo-electron tomography and biotin-streptavidin system. J Struct Biol 183, 305–311.

Oda T, Yagi T, Yanagisawa H, Kikkawa M (2013). Identification of the outer-inner dynein linker as a hub controller for axonemal dynein activities. Curr Biol 23, 656–664.

Oda T, Yanagisawa H, Kamiya R, Kikkawa M (2014a). Cilia and flagella molecular ruler determines the repeat length in eukaryotic cilia and flagella. Science 346, 857–886.

Oda T, Yanagisawa H, Yagi T, Kikkawa M (2014b). Mechanosignaling between central apparatus and radial spokes controls axonemal dynein activity. J Cell Biol 204, 807–819.

Pazour GJ, Rosenbaum JL (2002). Intraflagellar transport and cilia-dependent diseases. Trends Cell Biol 12, 551–555.

Perrone CA, Yang P, O'Toole E, Sale WS, Porter ME (1998). The Chlamydomonas IDA7 locus encodes a 140-kDa dynein intermediate chain required to assemble the I1 inner arm complex. Mol Biol Cell 9, 3351–3365.

Pettersen EF, Goddard TD, Huang CC, Couch GS, Greenblatt DM, Meng EC, Ferrin TE (2004). UCSF Chimera—a visualization system for exploratory research and analysis. J Comput Chem 25, 1605–1612.

Piperno G, Huang B, Luck DJ (1977). Two-dimensional analysis of flagellar proteins from wild-type and paralyzed mutants of Chlamydomonas reinhardtii. Proc Natl Acad Sci USA 74, 1600–1604.

Piperno G, Ramanis Z, Smith EF, Sale WS (1990). Three distinct inner dynein arms in Chlamydomonas flagella: molecular composition and location in the axoneme. J Cell Biol 110, 379–389.

Rupp G, Porter ME (2003). A subunit of the dynein regulatory complex in Chlamydomonas is a homologue of a growth arrest-specific gene product. J Cell Biol 162, 47–57.

Schleicher M, Watterson DM (1983). Analysis of differences between coomassie blue stain and silver stain procedures in polyacrylamide gels: conditions for the detection of calmodulin and troponin C. Anal Biochem 131, 312–317.

Summers KE, Gibbons IR (1971). Adenosine triphosphate-induced sliding of tubules in trypsin-treated flagella of sea-urchin sperm. Proc Natl Acad Sci USA 68, 3092–3096.

Warner FD (1976). Ciliary inter-microtubule bridges. J Cell Sci 20, 101–114.

Weber C, Lee VD, Chazin WJ, Huang B (1994). High level expression in Escherichia coli and characterization of the EF-hand calcium-binding protein caltractin. J Biol Chem 269, 15795–15802.

Wirschell M, Olbrich H, Werner C, Tritschler D, Bower R, Sale WS, Loges NT, Pennekamp P, Lindberg S, Stenram U, *et al.* (2013). The nexin-dynein regulatory complex subunit DRC1 is essential for motile cilia function in algae and humans. Nat Genet 45, 262–268.

Yanagisawa HA, Mathis G, Oda T, Hirono M, Richey EA, Ishikawa H, Marshall WF, Kikkawa M, Qin H (2014). FAP20 is an inner junction protein of doublet microtubules essential for both the planar asymmetrical waveform and stability of flagella in Chlamydomonas. Mol Biol Cell 25, 1472–1483.

Yang P, Diener DR, Rosenbaum JL, Sale WS (2001). Localization of calmodulin and dynein light chain LC8 in flagellar radial spokes. J Cell Biol 153, 1315–1326.